A Study of the Degradation of Electronic Speed Controllers for Brushless DC Motors

George E. Gorospe Jr.[1], Chetan S. Kulkarni[2], Edward Hogge[3], Andrew Hsu[4], and Natalie Ownby[5]

[1,2] *SGT Inc., NASA Ames Research Center, Moffett Field, CA 94035*
george.e.gorospe@nasa.gov
chetan.s.kulkarni@nasa.gov

[3] *Northrop Grumman Technical Services, Hampton, VA 23681*
edward.f.hogge@nasa.gov

[4] *NASA Postdoctoral Program, NASA Ames Research Center, Moffett Field, CA 94539*
andrew.hsu@nasa.gov

[5] *Texas State University - San Marcos, 601 University Dr. San Marcos, TX 7866*
nbo5@txstate.edu

ABSTRACT

Brushless DC motors are frequently used in electric aircraft and other direct drive applications. As these motors are not actually direct current machines but synchronous alternating current machines; they are electronically commutated by a power inverter. The power inverter for brushless DC motors typically used in small scale UAVs is a semiconductor based electronic commutator that is external to the motor and is referred to as an electronic speed control (ESC). This paper examines the performance changes of a UAV electric propulsion system resulting from ESC degradation. ESC performance is evaluated in simulation and on a new developed testbed featuring propulsion components from a reference UAV. An increase in the rise/fall times of the switched voltages is expected to cause timing issues at high motor speeds. This study paves the way for further development of diagnostic and prognostic methods for inverter circuits which are part of the overall electric UAV system.

1. INTRODUCTION

Electric propulsion systems for aircraft require reliability, resilience, and high power density. These systems must also manage weight, complexity, and operational costs. As more aircraft transition to electric propulsion systems, the management of faults and component degradation becomes increasingly important. In-Service data and performance data from degraded components supports diagnostic and prognostic methods for these systems but this data can be difficult to attain as weight and packaging restrictions reduce the instrumentation onboard aircraft. This paper is a study of the degradation of electronic speed controllers (ESCs) for permanent magnet brushless DC (PMBDC) motors through mathematical modeling, simulation, and laboratory testbed-based performance comparison of new and old controllers. This paper will focus only on the Jeti Opto Pro 90 series of ESCs used with PMBDC motors.

Among the electric motor technologies available for propulsion systems, the PMBDC motors have seen increased use in fields beyond hobby aircraft where they are ubiquitous due to their availability and low cost. PMBDC motors do not use an internal commutator and thus, are more efficient, offer higher torque to weight ratio, and typically run quieter than brushed dc motors. An aircraft propulsion system using PMBDC motors typically consists of an energy storage device such as a lithium polymer battery, ESCs to provide electric communication and frequency modulation based on control input, and the PMBDC motor which converts electrical energy to kinetic energy.

PMBDC machines are essentially synchronous machines with trapezoidal shaped induced emf. This simplifies the control and commutation of the current for these machines. To implement a control scheme for a PMBDC machine, only the beginning and the end of the flat portion of the induced electromotive force (emf) must be tracked, this results in six discrete positions by which two of the machine phases are

energized at any one moment (Krishnan, 2009). The ESC is responsible for monitoring these positions or modes, then switching the current accordingly. Reduced performance of an ESC due to degradation can have negative consequences on both the battery and the motor and could lead to a loss of thrust.

Previous work on fault diagnosis and health management for electric propulsion systems utilizing PMBDC motors has focused on open circuit winding faults and faults from malfunctioning transistor elements in power switching devices. Within transistor elements, both open-switch faults and low transistor base drive can lead to faulty conditions. To perform diagnostics on PMBDC dive systems, Park used a voltage sensor across the lower legs of the inverter to detect switch open-circuit faults, and fuses and switches to detect and mitigate switch short-circuit faults (Park, Kim, Ryu, & Hyun, 2006). Later, Park developed a diagnostic method by which the absolute value of the developed current on each leg of the inverter was monitored and summed, this sum was then compared with a threshold value (Park et al., 2011). Below the threshold value, the likelihood of fault conditions was high. Awadallah used a trained adaptive neuro-fuzzy inference system to not only detect the open switch fault, but identify the faulty switch (Awadallah & Morcos, 2006).

Other strategies for fault diagnosis and management have included the addition of supplementary phases (Gopalarathnam, Toliyat, & Moreira, 2000), techniques such as increasing current in healthy phases or extending conduction periods of healthy phases to make up for imbalances (Speed & Wallace, 1990), and methods for computing parameter changes expected during fault status. (Moseler & Isermann, 2000).

The following section outlines the motivation for this work. In section 3, the electric propulsion system model is described. This includes a model of the ESC power switching circuit and a model of a PMBLDC motor. Section 4 describes the development of two new testbeds for the evaluation of new and used ESCs both in isolation and the context of the full reference UAV propulsion system. This is followed by section 5 which covers the test sequences used for each testbed. In section 6 the results from both the simulation and the testbed experimentation are presented. Conclusions and future work are discussed in the final section

2. MOTIVATION

The motivation for this work evolved from flight operations with the all-electric Edge 540T UAV, where we observed abnormally high current draw from one of the batteries. This lead to a critical temperature increase in the motor windings. Investigation of the flight data and troubleshooting with batteries and other hardware confirmed that one of the ESC's on the UAV had degraded since the vehicle was commissioned and was drawing excess current resulting rise in motor winding temperature.

In our earlier work, we examined isolated components and performed component level prognostics (Celaya, Kulkarni, Biswas, Saha, & Goebel, 2011; Kulkarni, Celaya, Biswas, & Goebel, 2012). This has paved the way for the current work which focuses on the effects of component level degradation on the system as a whole. The development of new models and integration with previous models enables the simulation of an electric UAV propulsion system similar to that used in the Edge 540 electric UAV. This benefits research and development of a methodology for system level prognostics and has direct application to our continued operation of the Edge 540 for science missions. Within simulation, faults are injected into the operation of the ESC to observe the direct impacts on the components before and after the ESC in the system. In addition, two hardware-in-the-loop testbeds were developed to simulate flight loads on the propulsion system for experimentation with both a new ESC and a used ESC removed from the flight vehicle.

3. PROPULSION SYSTEM MODELING

This paper is focused on degradation observed in a Jeti Advance 90 Pro Opto electronic speed controller, commonly used in hobby electric propulsion systems. The advance 90 pro opto has a sustained current rating of 90 amps and a supply voltage range of 12 - 42 VDC. The speed controller is programmable, allowing the user to adjust the braking effect of the controller, the timing of the motor, acceleration rate, cut-off voltage and rotation direction. Furthermore, this model of speed controllers do not use motor sensors, such as hall effect sensors, for rotor position sensing. The modeled electric propulsion system as seen in the Fig. 1 shows key components which include a lithium-polymer battery as power source, an ESC consisting of a power conditioning circuit, gate driving circuit, and 3 phase power inverting circuit, and finally, a PMBDC motor.

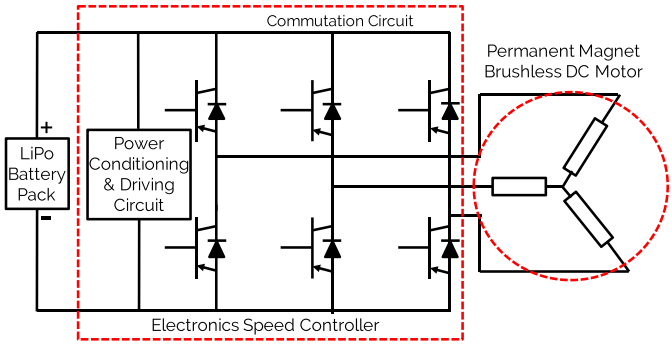

Figure 1. Schematic of an electric UAV propulsion system

In the next sub-section, we discuss models developed for the ESC and PMBDC motor respectively. The battery model and

conditioning circuit model are not discussed in this work. The developed models are then connected to form the electrical propulsion system.

3.1. Electronic Speed Control Circuits

For the purposes of this research, the ESC is modeled as an ideal power inverter employing sinusoidal pulse width modulation (SPWM) and half bridge drivers for each of three phases within a control block. Additionally, power switching devices are also modeled as ideal within the switching function block which represents the commutation functions of the ESC. This enables the study of switching faults, including open-circuit faults and short-circuit faults, and switching frequency faults. This modeling scheme is representative of general ESC operation for PMBDC motors which involves battery input, PWM input to control frequency, bridge drivers, and a semiconductor-based commutation circuit made up of switching transistors. To integrate these models with previous work they have been implemented in Simulink.

The control block implements a sinusoidal PWM control strategy as shown in which consists of a reference signal represented by a sine wave compared with a carrier signal represented by a triangle wave (C.Batard, Poitiers, Millet, & Ginot, 2012). This comparison creates a pulse width modulation (PWM) output that is high when the sine wave is larger than the triangle wave and low when it is not. There are 3 separate PWM generators within the control block. In each, the reference sine wave is shifted by 2PI/3 radians (Rao, Purna, Obulesh, & Babu, 2012). This shift in the sine wave creates a shift in the PWM outputs. The independence of each of the PWM generators allows faults to be modeled for one input without affecting the others. The output from the control block is connected to a switching function block. This switching function block also takes a constant voltage value representative of an ideal battery voltage and switching behavior matrix, m, which is used to model the switching behavior of the MOSFETS in the commutation circuit of the ESC. This matrix can be changed to simulate faults in the switching action of these elements.

$$m = \begin{bmatrix} 1 & -1 & 0 \\ 0 & 1 & -1 \\ -1 & 0 & 1 \end{bmatrix} \tag{1}$$

Within the switching function block, the PWM signals from the control block, F1, F2 and F3, are multiplied by the ideal voltage source V. This amplifies the PWM signal that drives the 3 phase inverter. This amplified PWM signal is then multiplied by the switching behavior matrix, m, to produce each leg of inverted power.

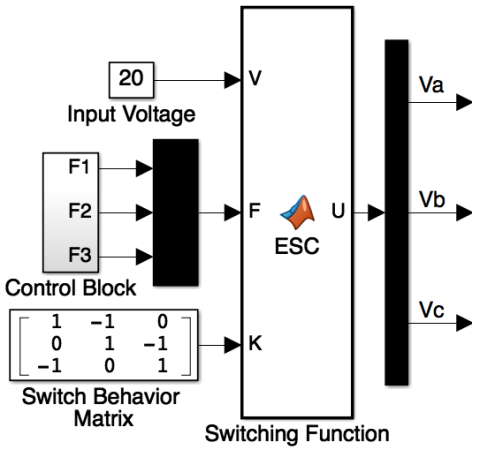

Figure 2. Developed ESC sim model

$$\begin{bmatrix} 1 & -1 & 0 \\ 0 & 1 & -1 \\ -1 & 0 & 1 \end{bmatrix} * V \begin{bmatrix} F1 \\ F2 \\ F3 \end{bmatrix} = \begin{bmatrix} v_{ab} \\ v_{bc} \\ v_{ca} \end{bmatrix} \tag{2}$$

The output of the function is a 3-phase voltage, Va, Vb, and Vc, that is then connected to the wye connected motor function block.

Within the control block, the frequency of the carrier wave used to create the PWM can also be changed. By decreasing the carrier signal frequency for a single leg of the inverter, a slower than normal switching action in the MOSFETS can be simulated. Additionally, the switch behavior matrix used in the function can also be manipulated to simulate faulty switching actions. In the original matrix, the values in the main diagonal are all 1, changing one of these values to 0 models the effect of having an open switch. For instance if the row 2 column 2 value is 0, the output of the ESC becomes [Vab; -Vb; Vca]. The developed model is used to both simulate nominal function of the ESC and a number of faulted scenarios. The data created by this model in simulation can be directly compared with empirical data from laboratory testing.

3.2. PMBDC Motor Dynamic Model

The brushless DC motor used in the testbed is an AC machine, which uses external electronic commutation provided by an electronic speed controller, instead of the internal mechanical commutation of brushed DC motors. Therefore, it has similar operating principles to permanent magnet synchronous machines, except with a trapezoidal, not sinusoidal, back-emf.

The dynamic model describes a three-phase brushless DC motor, with wye-connected stator windings and a permanent magnet as the rotor. This dynamic model only describes

the mechanical device, and assumes that the electronic speed controller provides a given input to the three-phase terminals.

Let the terminals of the wye-connection be labeled a,b, and c, and the center be labeled s. Each of the three windings are modeled as having a resistance, inductance, and back-emf voltage. Therefore, by applying KVL to each winding,

$$\begin{bmatrix} v_{as} \\ v_{bs} \\ v_{cs} \end{bmatrix} = \begin{bmatrix} R_a & 0 & 0 \\ 0 & R_b & 0 \\ 0 & 0 & R_c \end{bmatrix} \begin{bmatrix} i_a \\ i_b \\ i_c \end{bmatrix} + \frac{d}{dt} \begin{bmatrix} L_{aa} & L_{ab} & L_{ac} \\ L_{ba} & L_{bb} & L_{bc} \\ L_{ac} & L_{bc} & L_{cc} \end{bmatrix} \begin{bmatrix} i_a \\ i_b \\ i_c \end{bmatrix} + \begin{bmatrix} e_a \\ e_b \\ e_c \end{bmatrix}, \quad (3)$$

where v_{as}, v_{bs}, and v_{cs} refer to the stator phase voltages, R_a, R_a, and R_a refer to the stator winding resistances per phase, i_a, i_b and i_c are the currents flowing into each phase's terminal, and e_a, e_b and e_c are the back-emfs of each phase. In the case of the PMBDC motor, the back-emf voltages are trapezoidal and spaced apart at $2\pi/3$ radians. L_{aa}, L_{bb} and L_{cc} are the self inductances of each phase and L_{ab}, L_{bc} and L_{ac} are the mutual inductances between the three phases.

It is assumed that the resistances of each phase are equal, and that there is no salient rotor, so the self inductances are equal to each other, and the mutual inductances are equal to each other. Let the resistance of each phase be called R_s, the self inductances be called L, and the mutual inductances be M. Additionally, because of KCL, the currents i_a, i_b and i_c are balanced in the middle of the wye-connection, giving the constraint

$$i_a + i_b + i_c = 0. \quad (4)$$

If the mutual inductances are equal in all three phases, then Eq. 4 can be manipulated as

$$Mi_b + Mi_c = -Mi_a, \quad (5)$$

allowing Eq. 3 to be expressed as

$$\begin{bmatrix} v_{as} \\ v_{bs} \\ v_{cs} \end{bmatrix} = \begin{bmatrix} R_s & 0 & 0 \\ 0 & R_s & 0 \\ 0 & 0 & R_s \end{bmatrix} \begin{bmatrix} i_a \\ i_b \\ i_c \end{bmatrix} + \frac{d}{dt} \begin{bmatrix} L_M & 0 & 0 \\ 0 & L_M & 0 \\ 0 & 0 & L_M \end{bmatrix} \begin{bmatrix} i_a \\ i_b \\ i_c \end{bmatrix} + \begin{bmatrix} e_a \\ e_b \\ e_c \end{bmatrix}, \quad (6)$$

where $L_M = L - M$.

Eq. 6 models the dynamics of the currents in the three stator windings, but the mechanical motion of the motor must also be described. The electric torque generated by the back-emfs of the windings is the power divided by the rotational speed, ω_m. The power being transferred from the windings is the back-emf voltage, e_a, e_b and e_c, multiplied by each phase's respective current, i_a, i_b and i_c. Therefore, the electric torque is

$$T_e(e, i) = (e_a i_a + e_b i_b + e_c i_c)/\omega_m, \quad (7)$$

an algebraic function of the three phases' back-emfs and currents. Then, Newton's second law of motion gives us the dynamic equation for rotational speed,

$$\frac{d\omega_m}{dt} = \frac{1}{J}(-B\omega_m + (T_e(e, i) - T_l)), \quad (8)$$

where J is the inertia, B is the frictional coefficient, and T_l is the load torque on the rotor. Additionally, the rotor position, θ_m is

$$\frac{d\theta_m}{dt} = \frac{p}{2}\omega_m, \quad (9)$$

where p is the number of poles.

Finally, the voltages, v_{as}, v_{bs}, and v_{cs} are transformed from wye-connection to delta-connection variables. This is because the middle of the wye-connection is not an accessible voltage point, and the model intends to treat the input as terminal voltages v_a, v_b, and v_c.

Because the center of the wye-connection is one consistent point, let v_{ab} be simply $v_{as} - v_{bs}$, as well as $v_a - v_b$. Let the same principle apply for v_{bc} and v_{ac}. Then, Eq. 6 can be expressed as these delta-connection voltages,

$$\begin{bmatrix} v_{ab} \\ v_{bc} \\ v_{ac} \end{bmatrix} = \begin{bmatrix} R_s & -R_s & 0 \\ 0 & R_s & -R_s \\ R_s & 0 & -R_s \end{bmatrix} \begin{bmatrix} i_a \\ i_b \\ i_c \end{bmatrix} + \frac{d}{dt} \begin{bmatrix} L_M & -L_M & 0 \\ 0 & L_M & -L_M \\ L_M & 0 & -L_M \end{bmatrix} \begin{bmatrix} i_a \\ i_b \\ i_c \end{bmatrix} + \begin{bmatrix} e_a - e_b \\ e_b - e_c \\ e_a - e_c \end{bmatrix} \quad (10)$$

One may notice that v_{ac} is linearly dependent on v_{ab} and v_{bc}. This coincides with the constraint from Equation 4, which states that the three phase currents are also linearly dependent. The row corresponding to v_{ac} can be removed, and the variable i_c can be substituted with $-i_a - i_b$. Equation 10 can be simplified to

$$\begin{bmatrix} v_{ab} \\ v_{bc} \end{bmatrix} = R_s \begin{bmatrix} 1 & -1 \\ -1 & 2 \end{bmatrix} \begin{bmatrix} i_a \\ i_b \end{bmatrix} + L_M \begin{bmatrix} 1 & -1 \\ -1 & 2 \end{bmatrix} \frac{d}{dt} \begin{bmatrix} i_a \\ i_b \end{bmatrix} + \begin{bmatrix} e_a - e_b \\ e_b - e_c \end{bmatrix}, \quad (11)$$

leaving two sets of equations and only two currents as states. e_c remains and is known to be $2\pi/3$ radians out of phase with the other two back-emf voltages. The symmetry of resistances and inductances leaves a structure based on matrix $\begin{bmatrix} 1 & -1 \\ -1 & 2 \end{bmatrix}$. Inverting this matrix leaves $\begin{bmatrix} 2 & 1 \\ 1 & 1 \end{bmatrix}$, allowing Equation 11 to be expressed in terms of $\frac{di_a}{dt}$ and $\frac{di_b}{dt}$,

$$\frac{d}{dt} \begin{bmatrix} i_a \\ i_b \end{bmatrix} = -\frac{R_s}{L_M} \begin{bmatrix} i_a \\ i_b \end{bmatrix} + \frac{1}{L_M} \begin{bmatrix} 2 & 1 \\ 1 & 1 \end{bmatrix} \begin{bmatrix} v_{ab} \\ v_{bc} \end{bmatrix} - \frac{1}{L_M} \begin{bmatrix} 2 & -1 & -1 \\ 1 & 0 & -1 \end{bmatrix} \begin{bmatrix} e_a \\ e_b \\ e_c \end{bmatrix} \quad (12)$$

If the three phase input voltage and back-emf trapezoids are given, then Equations 8, 9, and 12 can be used as the dynamic equations of the brushless DC motor.

4. ELECTRIC PROPULSION TESTBED

Performance evaluation of the new and aged ESCs required the development of two different test systems. The first test system, the ESC testbed, isolates the speed controller and coupled motor to directly measure the 3 phase output of the ESC given a controlled DC input from a bench top power supply and PWM input from the data acquisition and control hardware (DAQ). This testbed was used for isolated ESC variable frequency no-load tests. The second test system, the electric propulsion testbed, isolates the electric propulsion system and provides additional instrumentation for the batteries, ESCs, and motor. This second test system was used for full propulsion system operation under constant load with flight-like RPM command.

Isolating the ESC and the motor in the ESC testbed eliminates variability from the batteries and enables the inclusion of a separate circuit for probing the signals created by the ESC. The ESC testbed relies on the addition of a star circuit composed of three 3.3 kOhm resistors in parallel to the three phase circuit circuit of the PMBDC motor. This star circuit creates a common reference point for each output phase and an individual test point for each phase. A laboratory bench top power supply provides a constant voltage of 20 VDC and a maximum of 15 amps to the ESC. A digital oscilloscope was used to probe each test point and capture the pulse train output for each phase from the ESC. This second test system isolates

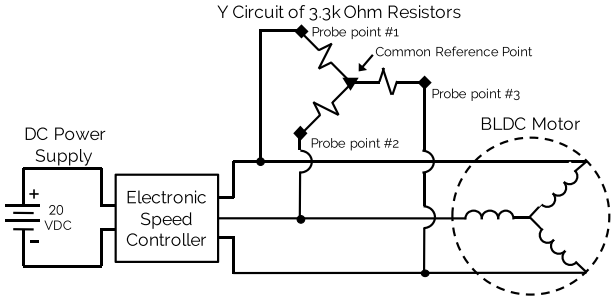

Figure 3. Isolated ESC test system

a copy of the propulsion system from the reference aircraft, the Edge 540T. The electric propulsion system testbed consists of two battery banks powering two ESCs connected to one double out-runner motor, a slave motor, instrumentation, and a data acquisition and control system (DAQ). The goal of this system is to generate flight-like loads on the propulsion system while utilizing increased instrumentation to generate data sets benefiting diagnostic and prognostic methods.

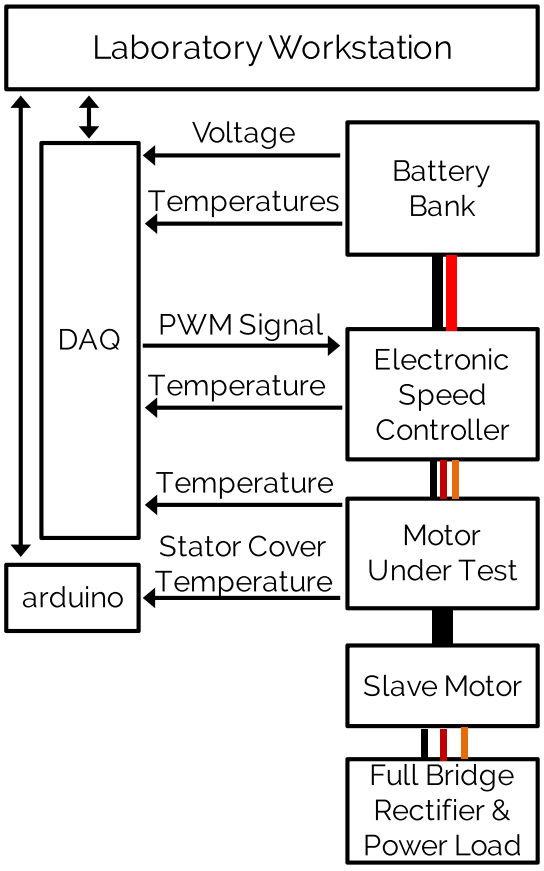

Figure 4. Isolated propulsion test system

Together this system and the software which commands the DAQ are able to playback flight data, commanding the ESCs

and the motor under test (MUT) to achieve the same RPM profile as the aircraft. While the isolated propulsion system mimics the aircraft flight thrust profile, instrumentation capture important trends in temperature, voltage, and current.

The isolated propulsion system testbed does not have any packaging or flight requirements, so additional instrumentation can be placed on components of interest. This system features individual battery voltage monitoring circuits, current monitoring hall effect sensors for each battery bank, thermocouples for direct temperature monitoring of the batteries, ESCs, and motor mount, and IR temperature sensors for non-contact temperature monitoring of the motor stator covers. A single National Instruments cDAQ captures data from these sensors, and produces a PWM signal for control of the ESCs. Additionally, an arduino is used to operate an optical tachometer and provide a I2C digital data bus for two thermopile temperature sensors used to monitor the rotating stator cover of each PMBDC motor without contact. The isolated propulsion system, sensors, and arduino are all located within a large fire resistant electrical junction box.

5. TEST SEQUENCE

Two different test sequences were used for the evaluation of ESC performance: isolated ESC variable frequency no-load operation and full propulsion system operation under constant load with variable RPM. The goal of each test sequence was to measure ESC performance under different duty cycles and flight conditions and overall system health. Both the new ESCs and the old ESCs were subject to the same tests.

During the isolated ESC variable frequency no-load tests, the ESCs were sequentially commanded from 10% throttle to 70% throttle in 7 increments. At each increment, the output of the ESC was measured using the star circuit and a digital oscilloscope. This sequence was completed for each ESC.

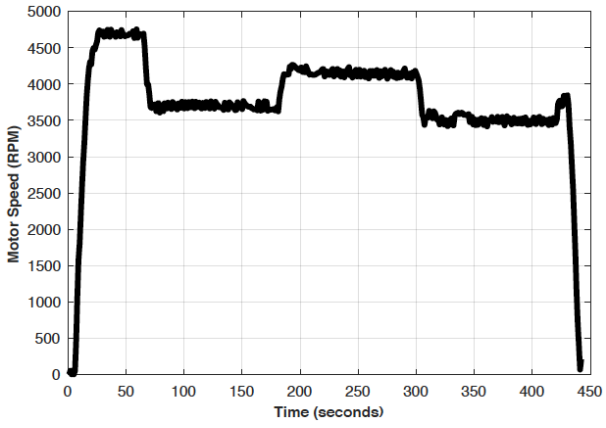

Figure 5. Abbreviated flight RPM data

During the full propulsion system operation under constant load with variable RPM, the propulsion system was commanded to achieve the RPM values of an flight profile abbreviated from 24 minutes to 7.5 minutes in length. This abbreviated flight profile contained take-off, mid-air maneuvers, and landing. For this test, the slave motor, full bridge rectifier and resistive load provided a constant mechanical load transferred to the propulsion system through a coupling of the motor and slave motor drive shafts. This test sequence was completed multiple times for both the new ESCs and the older, used ESCs. Between each test, the full propulsion system was allowed sufficient time to cool to a baseline temperature.

6. RESULTS

In this section we discuss the results obtained from simulating faults in the models as well as well results obtained from HIL testbed data.

6.1. Simulation Results

During simulation, the models were subject to two different faults which were injected into the ESC module. To observe how they affect the output of the ESC, nominal waveforms and faulted waveforms are compared. The ESC outputs are PWM waveforms which have a specific ON/OFF cycle depending on the requirements of the system. The following charts represent the voltage on the motor windings when a healthy ESC module is in operation and when a fault is injected. In all the simulations, the carrier frequency is 2 Hz and the switching matrix is as described in section 3.

The first simulated fault injected in the ESC module is a change in the PWM frequency, this is done to represent the slower switching action of degraded MOSFETs. This fault can be observed when the MOSFETs are out of synchronization during operation, resulting in a variation in the PWM output waveforms. Such waveforms may not be able to operate the BLDC motor efficiently, in addition the resulting harmonics may lead to increase in the internal temperature of the motor windings and an early failure of the motor. Fig. 6 presents a comparison of a normally operating ESC and an ESC with a PWM frequency fault injected causing a 5% reduction in switching frequency. In the plot it is observed that error does exist between the two waveforms.

Within the control block of the ESC, the 1^{st} PWM generator is faulted with a decreased frequency. This is representative of a fault in the switching action of the transistors which results in slower switching. Such a change in the controller could occur due to aging in the switching circuits. This may not occur as an abrupt fault but is an continuous degradation process which may start affecting the efficiency over the period of time. The other fault injected in the ESC module is a malfunction of the switching circuits in the commutation circuit. Fig. 7 represents the voltage output with a MOSFET malfunction fault injected. As observed from the plots, one

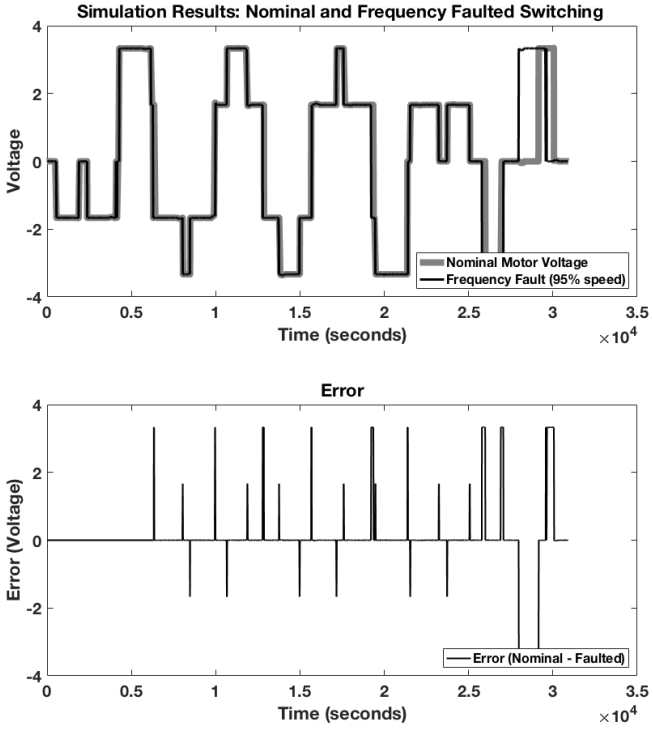

Figure 6. A comparison of nominal and frequency faulted ESC modules

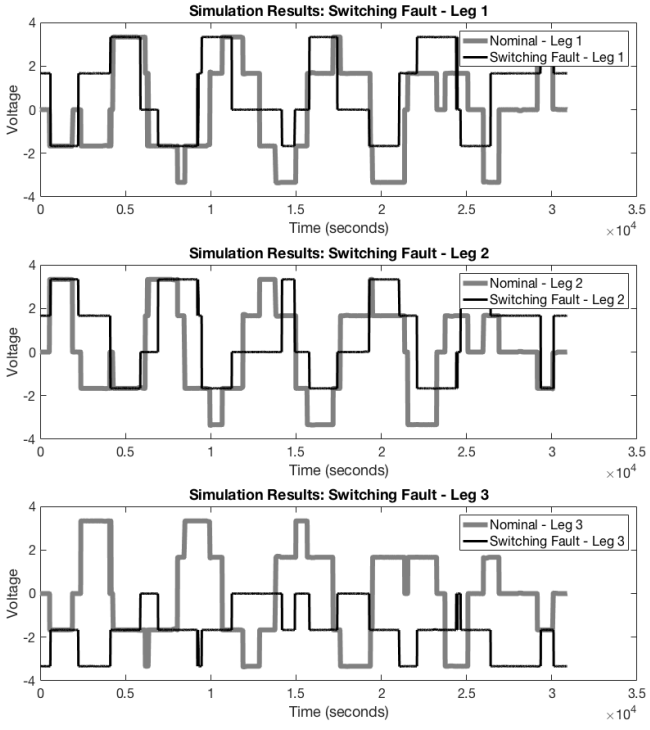

Figure 7. ESC output with switching fault on thrid leg

of the pair of MOSFETS is not operational due to a negative magnitude of the differential voltage Vab. This results in a out of sync waveforms which may lead to inefficient operation of the BLDC motor.

6.2. Hardware in Loop Results

The results from the hardware in the loop tests were collected during two test sequences, the first sequence isolated the ESCs from the full propulsion system, the second sequence measured the effects of the degraded ESC on the other components of the propulsion system. In Fig. 8, the measured voltage potential across one leg of the 3.3 kOhm Y circuit is presented. This figure is characteristic of the results from the isolated ESC variable-frequency no-load test sequence. Here, the Y circuit is in parallel with the PMBDC motor and shows the evolved voltage during commutation. The shape of the evolved voltage seems to suggest switching performance degradation. There is also a clear discrepancy between the produced voltages of the new and old ESCs given identical inputs.

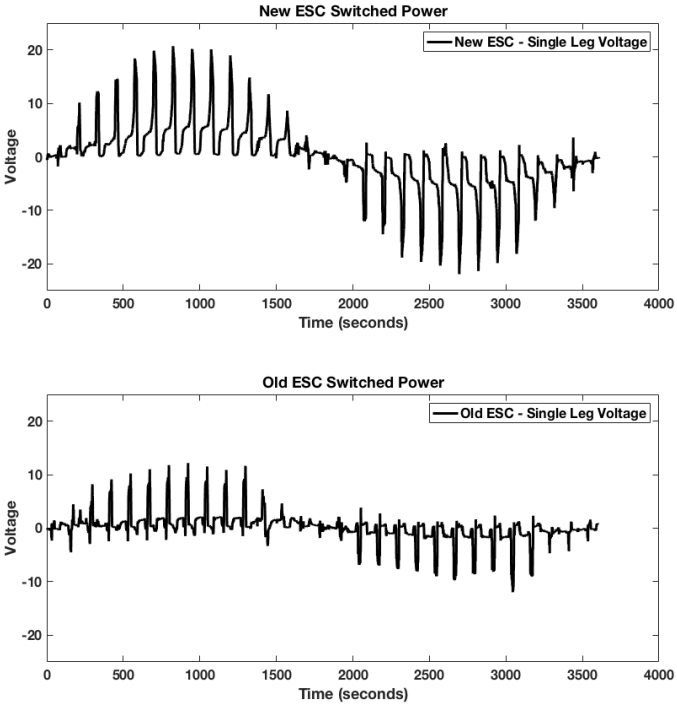

Figure 8. A compairson of output signals from new and old ESCs

The next two figures present the voltage drop during flight-like loading for both the new and the old ESCs. During these tests, the system was commanded to achieve motor velocity equal to the RPM set point under a fixed mechanical load. In each chart the voltage drop measured across the battery bank is labeled. It was expected that the older ESC would cause a greater drop. However, given the limited samples it is not clear that this is the case.

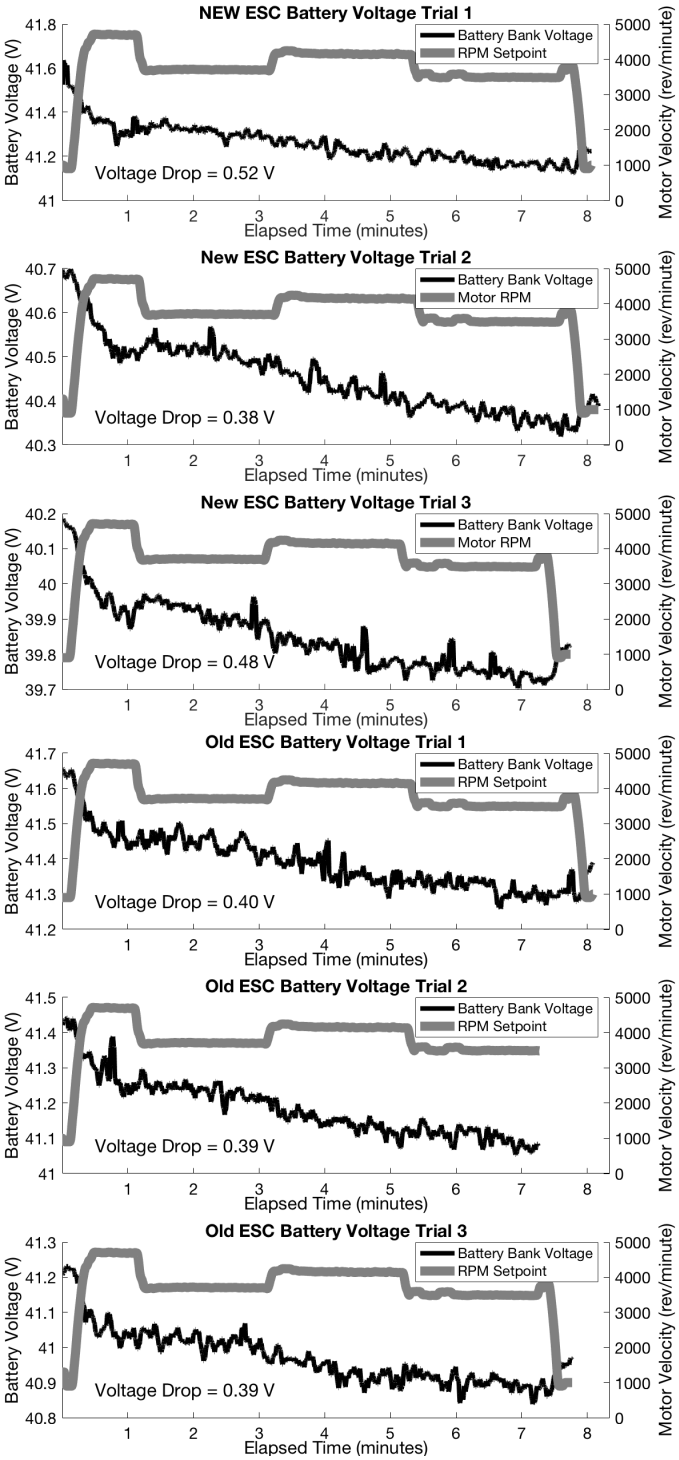

Figure 9. Battery discharge curve for the new & old ESC

The next few figures present the resulting temperature changes of other elements of the propulsion system including the batteries, motor, and the ESCs themselves. During 6 total trials, 3 trials with the degraded ESCs and 3 trials with new ESCs, we measured the component temperature change.

Figure 10 shows the temperature change in each of the two lithium polymer batteries in series and connected to the ESC. In most cases, the first battery in series experiences a larger rise in temperature. No significant temperature differences were detected between the batteries used with new and old ESC. Figure 11 presents the resulting temperature change of

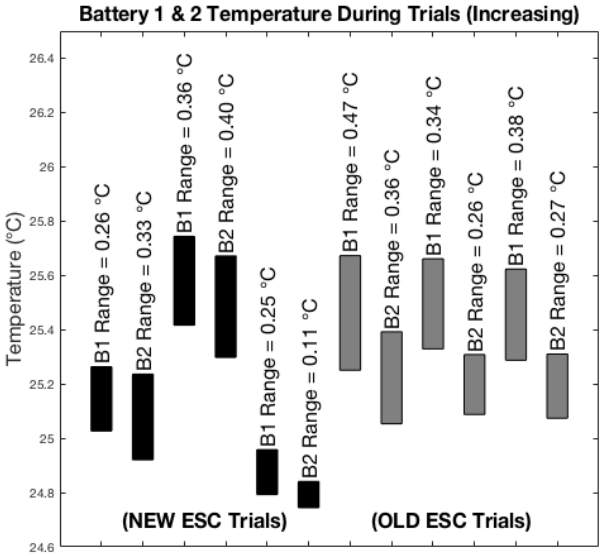

Figure 10. Temperature change in batteries 1 & 2 used to power the ESC during trials

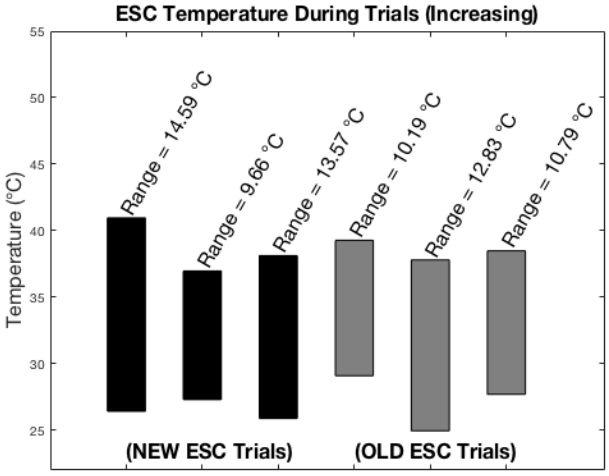

Figure 11. Temperature change in new and old ESCs during trials

the ESC during testing. The temperature was measured at the junction between the ESC and it's heat sink. No clear trend is visible from these results.

Figure 12 presents the resulting temperature change of the motor stator cover during tests. The motor stator cover experienced some of the highest increases in temperature during tests and although no clear trend in the temperature data is

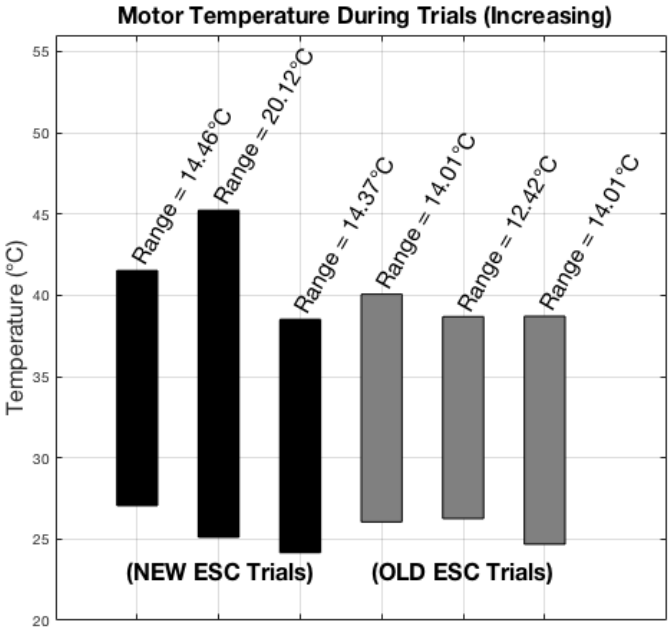

Figure 12. Temperature change in the motor stator cover during trials

shown here we expect that longer tests may reveal a saturation point at which the temperature no longer increases.

7. CONCLUSION

Through mathematical modeling, simulation and laboratory bench top testing, we have studied ESC degradation in isolation and in the context of a full electric propulsion system characteristic of those used commonly on small UAVs. We also coupled a new model of the ESC with a model of a PMBDC motor and explored switching faults and frequency faults. Both simulation and laboratory bench top testing yielded new data which can be used for the maturation of new prognostic methods focusing on ESCs and the electronic commutation of direct current for PMBDC motors. The ESC model provided an insight to the commutation circuit and how output could change if a fault were developing. The hardware in the loop testbed allowed us to see which performance metrics of the propulsion system were clearly effected by degradation in the ESCs and which metrics had subtler changes. The evolved voltage from the older ESCs shows clear signs of degradation when compared to the output of the new ESC. More testing is necessary to make any conclusions towards the effect of degraded ESCs on the temperature of coupled propulsion components.

Future work on this project will focus on the continued development of the mathematical model of the ESC and improvements towards the functionality and instrumentation of the hardware-in-the-loop testbed. We intend to include more components, such as the gate drivers into the next model of the ESC. We will also use data from laboratory testing to refine the behavior of the model. Improvements to the HITL testbed will include new circuits to reduce noise in the current measurement circuit, a measurement of the throttle level applied and resultant RPM, a more precise measurement of the motor stator cover temperature, and a means for dynamically adjusting the mechanical load on the motor under test. Finally, with a more mature testbed, we intend to perform many more loaded tests of the full testbed to better understand the effects of ESC degradation on coupled components.

REFERENCES

Awadallah, M. A., & Morcos, M. M. (2006). Automatic diagnosis and location of open-switch fault in brushless dc motor drives using wavelets and neuro-fuzzy systems. *IEEE Transactions on Energy conversion*, *21*(1), 104–111.

C.Batard, Poitiers, F., Millet, C., & Ginot, N. (2012, September). Simulation of power converters using matlab-simulink. *INTECH*, *1*.

Celaya, J. R., Kulkarni, C., Biswas, G., Saha, S., & Goebel, K. (2011). A model-based prognostics methodology for electrolytic capacitors based on electrical overstress accelerated aging. In *Proceeding of annual conference of the prognostics and health management society* (pp. 1–9).

Gopalarathnam, T., Toliyat, H. A., & Moreira, J. C. (2000). Multi-phase fault-tolerant brushless dc motor drives. In *Industry applications conference, 2000. conference record of the 2000 ieee* (Vol. 3, pp. 1683–1688).

Krishnan, R. (2009). *Permanent magnet synchronous and brushless dc motor drives*. CRC Press.

Kulkarni, C. S., Celaya, J. R., Biswas, G., & Goebel, K. (2012). Towards a model-based prognostics methodology for electrolytic capacitors: A case study based on electrical overstress accelerated aging. *International Journal of Prognostics and Health Management*, *5*(1), 16.

Moseler, O., & Isermann, R. (2000). Application of model-based fault detection to a brushless dc motor. *IEEE Transactions on industrial electronics*, *47*(5), 1015–1020.

Park, B.-G., Kim, T.-S., Ryu, J.-S., & Hyun, D.-S. (2006). Fault tolerant strategies for bldc motor drives under switch faults. In *Industry applications conference, 2006. 41st ias annual meeting. conference record of the 2006 ieee* (Vol. 4, pp. 1637–1641).

Park, B.-G., Lee, K.-J., Kim, R.-Y., Kim, T.-S., Ryu, J.-S., & Hyun, D.-S. (2011). Simple fault diagnosis based on operating characteristic of brushless direct-current motor drives. *IEEE Transactions on Industrial Electronics*, *58*(5), 1586–1593.

Rao, A., Purna, C., Obulesh, Y. P., & Babu, C. S. (2012).

Mathematical modeling of bldc motor with closed loop speed control using pid controllers under various loading conditions. *ARPN Journal of Applied Sciences and Engineering*.

Speed, R., & Wallace, A. K. (1990). Remedial strategies for brushless dc drive failures. *IEEE Transactions on industry Applications*, *26*(2), 259–266.